Available online at www.sciencedirect.com
SciVerse ScienceDirect
Acta Materialia 61 (2013) 4354–4364
Acta MATERIALIA
www.elsevier.com/locate/actamat

Stress generation during lithiation of high-capacity electrode particles in lithium ion batteries

S. Huang [a], F. Fan [a], J. Li [b,c], S. Zhang [d], T. Zhu [a,*]

[a] *Woodruff School of Mechanical Engineering, Georgia Institute of Technology, Atlanta, GA 30332, USA*
[b] *Department of Nuclear Science and Engineering, Massachusetts Institute of Technology, Cambridge, MA 02139, USA*
[c] *Department of Materials Science and Engineering, Massachusetts Institute of Technology, Cambridge, MA 02139, USA*
[d] *Department of Engineering Science and Mechanics, Pennsylvania State University, University Park, PA 16802, USA*

Received 1 August 2012; received in revised form 19 March 2013; accepted 4 April 2013
Available online 3 May 2013

Abstract

A model is developed to study the stress generation in a spherical particle subjected to lithium insertion. The model accounts for both the plastic deformation and the coexistence of lithium-poor and lithium-rich phases with a sharp and curved phase boundary. Such two-phase and inelastic deformation characteristics often arise during lithiation of crystalline particles with high capacity. A flexible sigmoid function is used to create the lithium profile with a step-like change in lithium concentration, mimicking a sharp phase boundary that separates a pristine core and a lithiated shell in the particle. The mechanics results, obtained by an analytic formulation and finite difference calculations, show the development of tensile hoop stress in the surface layer of the lithiated shell. This hoop tension provides the driving force of surface cracking, as observed by in situ transmission electron microscopy. The two-phase lithiation model is further compared with the single-phase one, which assumes a gradual and smooth variation in radial lithium distributions, and thus predicts only hoop compression in the surface layer of the particle. Furthermore, the effect of dilatational vs. unidirectional lithiation strains in the two-phase model is studied, thereby underscoring the critical role of anisotropy of lithiation strain in controlling stress generation in high-capacity electrodes for lithium ion batteries.

Keywords: Lithium ion battery; Lithiation-induced stress; Solid-state electrode; Two-phase microstructure

1. Introduction

Lithium ion batteries (LIB) are critically important for providing energy to portable electronic devices and transportation vehicles [1–4]. To achieve a higher energy density in LIB, new anode materials, such as silicon and its composites, are being intensively studied as potential replacements for the currently used graphite [5–8]. One critical issue associated with those high-capacity electrodes is the large volume change during Li insertion and extraction, e.g., ~310% for Si. The resulting high stresses can cause fracture and pulverization of electrodes, thus leading to loss of electrical contact and limiting the cycle life of LIB. To address these issues, it is essential to understanding how the stress arises and evolves in the lithiated materials.

Recent experiments indicate that plastic deformation can readily occur in high-capacity electrodes during lithiation [9–15]. Interestingly, in situ transmission electron microscopy (TEM) experiments reveal that lithiation often proceeds through movement of an atomically sharp phase boundary that separates the lithiated and unlithiated material [10,11,16–18]. For example, the TEM images in Fig. 1 show the formation of a core–shell structure in a partially lithiated Si nanoparticle, which consists of a two-phase boundary that separates an inner core of crystalline Si with

---

* Corresponding author. Tel.: +1 404 894 6597.
E-mail address: ting.zhu@me.gatech.edu (T. Zhu).

1359-6454/$36.00 © 2013 Acta Materialia Inc. Published by Elsevier Ltd. All rights reserved.
http://dx.doi.org/10.1016/j.actamat.2013.04.007

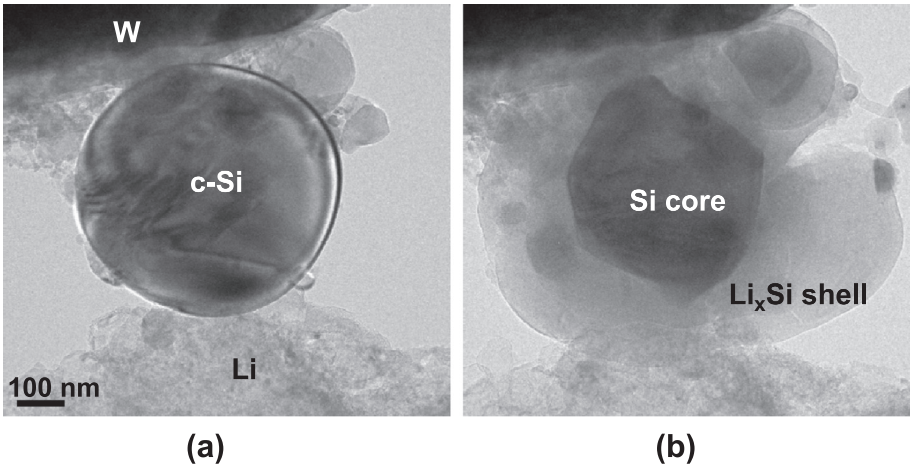

Fig. 1. In situ TEM observation of lithiation and cracking in a Si nanoparticle, adapted from Refs. [14,15]. (a) A crystalline Si (c-Si) nanoparticle is in contact with a tungsten (W) electrode and a Li metal counter electrode, whose surface is covered with Li_2O that acts as a solid electrolyte. (b) Under an applied voltage between the two electrodes, Li quickly covers the particle surface and then flows radially into the particle, forming the structure of a pristine inner Si core (black) and an amorphous Li_xSi ($x \approx 3.75$) alloy shell (gray) with a sharp interface in-between. The lithiation-induced swelling causes crack initiation from the particle surface.

an outer shell of amorphous Li_xSi ($x \approx 3.75$). The observation of such a sharp phase boundary suggests that the Li-poor and Li-rich phases do not transform continuously into each other with changing composition, i.e., there is a large solubility gap Δx between the two phases, manifested as an abrupt change in Li concentrations across the phase boundary. Moreover, Fig. 1b reveals the formation of a surface crack, indicating the development of hoop tension in the surface layer during Li insertion. While theoretical models have been developed to analyze the Li diffusion, reaction and associated stress states in lithiated materials [19–40], the effects of plastic deformation and two-phase microstructures on stress generation are not yet well understood. The present paper reports on a theoretical model that accounts for both factors.

Nanomaterials, such as nanoparticles and nanowires, are being intensively studied as the basic building blocks of electrodes for LIB [41]. This is motivated by the notion that the nanometer size scale can shorten the diffusion path and enable facile strain relaxation, thus enhancing both the rate capability and flaw tolerance of the nanomaterial-based electrodes [7,42–43]. The present work focuses on the stress generation associated with a curved two-phase boundary, i.e., core–shell interface, which arises frequently during lithiation of nanoparticles and nanowires. It is important to note that lithiation at a moving core–shell interface affects not only the local stress states, but also the stresses in materials behind the moving boundary [11,13,14]. This may have a dramatic effect on the fracture behavior of lithiated nanoparticles, e.g., leading to cracking in the outer surface during Li insertion, as shown in Fig. 1b. While the stress generation and surface cracking have been modeled by finite element simulations in previous publications [11,14], the present paper reports a systematic mechanics study of a core–shell particle based on the analytic formulation and finite difference numerical simulations. The results provide a transparent mechanics foundation for a more direct physical understanding of stress generation during lithiation of high-capacity electrode materials with curved geometries.

The organization of the paper is as follows. Section 2 reviews a general mechanics model of the lithiation-induced elastic–plastic deformation and stress. Based on this mechanics framework, an analytic formulation and associated numerical procedures are developed in Section 3 to solve the stress distribution in a lithiated spherical particle. In Section 4, the numerical results of stress generation are presented for a core–shell particle with a sharp two-phase boundary, and a direct physical appreciation of the origin of hoop tension in the surface layer during lithiation is then provided. In this section, the stress distributions in a single-phase particle with gradually varying Li profiles are also obtained, highlighting the differences in stress generation between the two-phase and single-phase lithiation mechanisms. In addition, the effects of dilational vs. unidirectional lithiation strains on stress states are studied. The concluding remarks are given in Section 5. The Appendix describes how the mechanics model in Section 2 is implemented in the ABAQUS finite element package, and the associated numerical results validate those given in the text.

2. A mechanics model of lithiation

To focus on the essential physical effects of lithiation on stress generation, a simple elastic–plastic model is adopted to evaluate the deformation and stress states during Li insertion [27]. The total strain rate $\dot{\varepsilon}_{ij}$ is taken to be the sum of three contributions

$$\dot{\varepsilon}_{ij} = \dot{\varepsilon}^c_{ij} + \dot{\varepsilon}^e_{ij} + \dot{\varepsilon}^p_{ij} \tag{1}$$

where $\dot{\varepsilon}_{ij}^{c}$ is the chemical strain rate caused by lithiation and is proportional to the rate of the normalized Li concentration $\dot{c}$

$$\dot{\varepsilon}_{ij}^{c} = \beta_{ij}\dot{c} \tag{2}$$

where β_{ij} is the lithiation expansion coefficient, and c varies between 0 (pristine Si) and 1 (fully lithiated $\mathrm{Li}_{3.75}\mathrm{Si}$). In Eq. (1), $\dot{\varepsilon}_{ij}^{e}$ denotes the elastic strain rate and obeys Hooke's law

$$\dot{\varepsilon}_{ij}^{e} = \frac{1}{E}[(1+v)\dot{\sigma}_{ij} - v\dot{\sigma}_{kk}\delta_{ij}] \tag{3}$$

where E is Young's modulus, v is Poisson's ratio, $\delta_{ij} = 1$ when $i = j$ and $\delta_{ij} = 0$ otherwise, and repeated indices mean summation. In Eq. (1), the plastic strain rate $\dot{\varepsilon}_{ij}^{p}$ obeys the classic J_2-flow rule: that is, plastic yielding occurs when the effective stress, $\sigma_e = \sqrt{3\sigma_{ij}'\sigma_{ij}'/2}$, equals the yield strength σ_Y, where $\sigma_{ij}' = \sigma_{ij} - \sigma_{kk}\delta_{ij}/3$ is the deviatoric stress. The plastic strain rate is given by

$$\dot{\varepsilon}_{ij}^{p} = \dot{\lambda}\sigma_{ij}' \tag{4}$$

where $\dot{\lambda}$ is a scalar coefficient and can be determined as described in Section 3.

3. Elastic–plastic deformation in a lithiated particle with two phases

3.1. Two-phase boundary

To study the microstructural evolution in a multiphase material, one generally needs to model diffusion in each phase as well as migration of phase boundaries [44,45]. Since this work is focused on the stress generation in a core–shell particle rather than the detailed dynamics of the evolving multiphase microstructures [28], a series of one-dimensional step-like profiles of Li distribution are directly created, which mimic the movement of a sharp phase boundary between the Si core and the $\mathrm{Li}_{3.75}\mathrm{Si}$ shell. Such Li distribution is created with a flexible sigmoid function (so-called generalized logistic function) that is widely used for growth modeling

$$c(r) = \frac{1}{[1 + Qe^{-B(r-r_c)}]^{1/\alpha}} \tag{5}$$

Eq. (5) allows flexible control of the Li distribution near the two-phase boundary, as well as the time law of boundary migration. The logistic function in Eq. (5) has two asymptotic limits of $c = 0$ and 1, representing the pristine Si core and $\mathrm{Li}_{3.75}\mathrm{Si}$ shell, respectively; B dictates the sharpness of the Li concentration jump from 0 to 1; $\alpha > 0$ affects the concentration profile near the asymptote maximum and is taken as unity for simplification in this work; Q is similarly taken as unity. Since r_c approximately represents the center of the two-phase boundary (where $c = 0.5$), one can prescribe different time laws of $r_c(t)$ to move the phase boundary from the particle surface ($r_c = 1$) to its center ($r_c = 0$). Correspondingly, different spatial–temporal variations of Li concentration, $\dot{c}(r, t)$, can be obtained for the study of stress generation, as described next. Physically, the lithiation involves two processes in series: (1) the Li diffusion through the lithiated shell already formed; and (2) the chemical reaction at the two-phase boundary. The prescribed time law for the moving interface could represent either the lithiation that is rate-limited by the reaction at the phase boundary or the Li diffusion-limited case in the steady state when the Li flux in the lithiated shell is balanced with the reaction rate at the phase boundary; these different rate-limiting steps have been discussed in the study of Si oxidation [46] and Si lithiation [37–40].

3.2. Mechanics formulation

The mechanics model described in Section 2 is applied to study the lithiation-induced stresses in a spherical particle. Assuming the deformation is spherically symmetric, an analytic formulation is first developed, and then the finite difference method is used to solve the stress distribution. In a spherical coordinate system (r, θ, φ), the strain rate of Eq. (1) can be written as

$$\dot{\varepsilon}_r = \dot{\varepsilon}_r^c + \dot{\varepsilon}_r^e + \dot{\varepsilon}_r^p, \quad \dot{\varepsilon}_\theta = \dot{\varepsilon}_\varphi = \dot{\varepsilon}_\theta^c + \dot{\varepsilon}_\theta^e + \dot{\varepsilon}_\theta^p \tag{6}$$

The chemical strain rate of Eq. (2) is given by

$$\dot{\varepsilon}_r^c = \beta_r\dot{c}, \quad \dot{\varepsilon}_\theta^c = \dot{\varepsilon}_\varphi^c = \beta_\theta\dot{c} \tag{7}$$

Here, it is assumed $\beta_\theta = \beta_\varphi$, so as to maintain the spherically symmetrical deformation. It follows that the elastic strain rate of Eq. (3) is rewritten as

$$\dot{\sigma}_r = \frac{E}{(1+v)(1-2v)}[(1-v)\dot{\varepsilon}_r^e + 2v\dot{\varepsilon}_\theta^e],$$
$$\dot{\sigma}_\theta = \dot{\sigma}_\varphi = \frac{E}{(1+v)(1-2v)}[\dot{\varepsilon}_\theta^e + v\dot{\varepsilon}_r^e] \tag{8}$$

The plastic strain rate of Eq. (4) is given by

$$\dot{\varepsilon}_r^p = \dot{\bar{\varepsilon}}^p\frac{3\sigma_r'}{2\sigma_e}, \quad \dot{\varepsilon}_\theta^p = \dot{\varepsilon}_\varphi^p = \dot{\bar{\varepsilon}}^p\frac{3\sigma_\theta'}{2\sigma_e} \tag{9}$$

where the deviatoric stresses are

$$\sigma_r' = \frac{2}{3}(\sigma_r - \sigma_\theta), \quad \sigma_\theta' = \sigma_\varphi' = \frac{1}{3}(\sigma_\theta - \sigma_r) \tag{10}$$

and the effective stress is

$$\sigma_e = \sqrt{\frac{3}{2}\sigma_{ij}'\sigma_{ij}'} = |\sigma_r - \sigma_\theta| \tag{11}$$

To stabilize the numerical calculation involving a sharp interface, it is assumed that the plastic deformation is rate dependent, and the rate-independent limit is obtained by taking a vanishingly small value of rate sensitivity. Specifically, the effective plastic strain rate is

$$\dot{\bar{\varepsilon}}^p = \dot{\bar{\varepsilon}}_0^p\left(\frac{\sigma_e}{s}\right)^{1/m} \tag{12}$$

where $\dot{\bar{\varepsilon}}_0^p$ is an effective strain rate constant, s is the plastic flow resistance, and m is the rate sensitivity exponent. In the limit of the rate-independent deformation, $m \to 0$ and

$\sigma_e \rightarrow s$. In Eq. (12), s is often taken as a function of the accumulated plastic strain to model the strain hardening [47]. Here, constant $s = \sigma_Y$ is assumed, corresponding to perfectly plastic deformation. In the case of spherically symmetrical deformation, the governing equilibrium equation is simplified as

$$\frac{d\dot{\sigma}_r}{dr} + \frac{2}{r}(\dot{\sigma}_r - \dot{\sigma}_\theta) = 0 \tag{13}$$

The strain rates are related to the radial velocity V_r according to

$$\dot{\varepsilon}_r = \frac{dV_r}{dr}, \quad \dot{\varepsilon}_\theta = \dot{\varepsilon}_\varphi = \frac{V_r}{r} \tag{14}$$

For a free-standing particle with radius R, the boundary conditions involve zero traction at the surface

$$\dot{\sigma}_r(r = R) = 0 \tag{15}$$

and zero velocity at the center

$$V_r(r = 0) = 0 \tag{16}$$

3.3. Finite difference method

Based on the analytic formulation in Section 3.2, the lithiation-induced stresses in a spherical particle are solved using the finite difference method. Combining Eqs. (6), (8), and (14), one can express the stress rates in terms of the radial velocity V_r

$$\dot{\sigma}_r = \frac{E}{(1+v)(1-2v)}\left[(1-v)\left(\frac{dV_r}{dr} - \dot{\varepsilon}_r^c - \dot{\varepsilon}_r^p\right) + 2v\left(\frac{V_r}{r} - \dot{\varepsilon}_\theta^c - \dot{\varepsilon}_\theta^p\right)\right] \tag{17}$$

$$\dot{\sigma}_r - \dot{\sigma}_\theta = \frac{E(1-2v)}{(1+v)(1-2v)}\left[\frac{dV_r}{dr} - \frac{V_r}{r} - \dot{\varepsilon}_r^c - \dot{\varepsilon}_r^p + \dot{\varepsilon}_\theta^c + \dot{\varepsilon}_\theta^p\right] \tag{18}$$

Substitution of Eqs. (17) and (18) into Eq. (13) gives the equilibrium equation in terms of V_r

$$\frac{d^2V_r}{dr^2} + \frac{2}{r}\frac{dV_r}{dr} - \frac{2V_r}{r^2} = \frac{1}{1-v}\frac{d}{dr}[(1-v)(\dot{\varepsilon}_r^c + \dot{\varepsilon}_r^p) + 2v(\dot{\varepsilon}_\theta^c + \dot{\varepsilon}_\theta^p)] + \frac{2(1-2v)}{1-v}\frac{1}{r}[(\dot{\varepsilon}_r^c + \dot{\varepsilon}_r^p) - (\dot{\varepsilon}_\theta^c + \dot{\varepsilon}_\theta^p)] \tag{19}$$

Suppose both the chemical and plastic strain rates are known at time t, Eq. (19) becomes a second-order ordinary differential equation of V_r, enabling one to determine its radial distribution at time t using the finite difference and iterative shooting methods. Specifically, the radial distance of a spherical particle is discretized into n points $r^{(i)} \in [0, R]$, $(i = 1, \ldots, n)$, with equal spacing $\Delta r = R/(n-1)$, and then Eq. (19) is discretized by the finite difference relations

$$\frac{d^2V_r}{dr^2} = \frac{V_r^{(i+1)} + V_r^{(i-1)} - 2V_r^{(i)}}{(\Delta r)^2}, \quad \frac{dV_r}{dr} = \frac{V_r^{(i+1)} - V_r^{(i-1)}}{2\Delta r} \tag{20}$$

where $V_r^{(i)}$ is the radial velocity at $r^{(i)}$. To determine $V_r^{(i)}$ at time t, one starts with $V_r^{(1)}(r^{(1)} = 0) = 0$, as dictated by the boundary condition of Eq. (16), makes an initial guess of $V_r^{(2)}$, solves $V_r^{(3)} \ldots V_r^{(N)}$ based on Eqs. (19) and (20), and then calculates $\dot{\sigma}_r(r = R)$ according to Eq. (17). In order to satisfy the traction-free boundary condition of Eq. (15), the above calculations are repeated to find the optimal $V_r^{(2)}$ that gives $\dot{\sigma}_r(r = R)$ closest to zero, thus enabling the update of $V_r^{(i)}$ at time t. It follows that all the stress rates at time t are calculated based on Eqs. (17) and (18), and then all the plastic strain rates are updated at time $t + \Delta t$ based on Eqs. (9)–(12). Suppose the chemical strain rate at time $t + \Delta t$ is known from Eq. (7) and $\dot{c}$ at $t + \Delta t$ on the basis of a prescribed time law, one can repeat the above steps to determine $V_r^{(i)}$ at $t + \Delta t$, thereby accomplishing one loop of numerical integration.

4. Results and discussion

4.1. Two-phase particle

Fig. 2a shows the representative results of radial Li distribution with a sharp phase boundary, created using the logistic function of Eq. (5) with $B = 80$. Since the present study is focused on the rate-independent limit of elastic–plastic deformation, a simple time law of $r_c(t) \propto t$ is assumed to move the phase boundary from the particle surface to its center.

Based on the analytic formulation in Section 3.2 and the finite difference method in Section 3.3, the stress distributions associated with the movement of a two-phase boundary are evaluated as shown in Fig. 2b and c. The material properties that are representative of high-capacity electrode materials such as Si—yield stress $\sigma_Y = 0.05E$ and Poisson's ratio $v = 0.3$—are chosen. It is important to emphasize that a physical assignment of lithiation strains is not yet possible because of the lack of experimental measurement. Assuming the dilational lithiation strains, taking the lithiation expansion coefficients $\beta_r = \beta_\theta = \beta_\varphi = 0.26$ yields a volume increase by ~100%. Effects of lithiation strains on the stress generation will be further studied later by examining the case of unidirectional lithiation strain in the radial direction. In addition, the rate sensitivity exponent $m = 0.01$ is taken to approximate the rate-independent limit, and the effective strain rate constant $\dot{\bar{\varepsilon}}_0^p = 0.001$. Notably, the radial stress σ_r at the particle surface has been kept at zero using the iterative shooting method (Section 3.3).

Fig. 2b and c shows the simulated results of radial stress distributions corresponding to the Li profiles in Fig. 2a. The most salient feature is the development of the tensile hoop stress in the surface layer in the late stage of lithiation, as seen from Fig. 2c, and such hoop tension reverses the initial compression that is shown in Fig. 2b. Correspondingly, the core is first subjected to hydrostatic tension and later changed to hydrostatic compression. This change results from the buildup of hoop tension in the surface layer, as well as the requirement that the resultant of normal stresses over any diameter plane in a free-standing spherical particle must be zero.

To provide a direct physical appreciation of the reversal of hoop compression to tension in the surface layer, Fig. 3 shows the schematics of the hoop stress experienced by a representative material element A in the surface layer of a

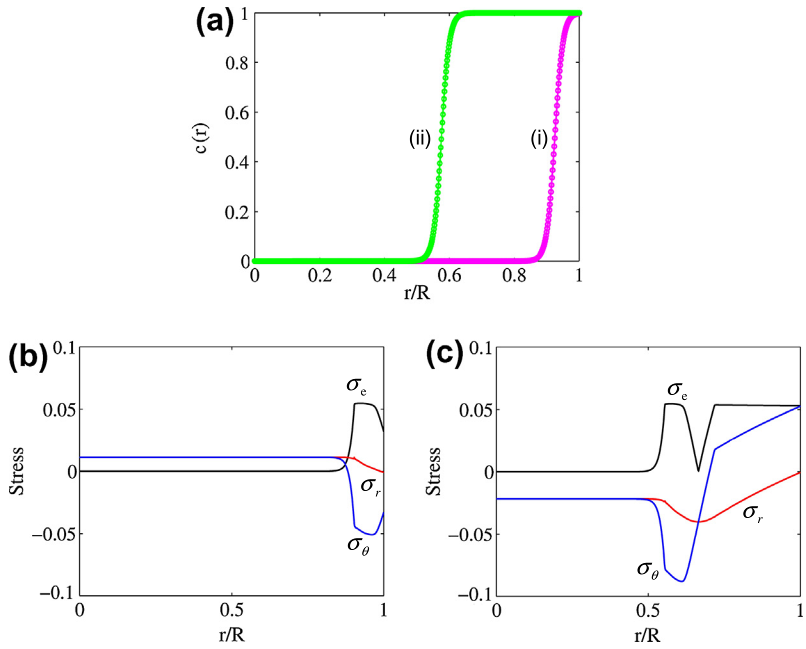

Fig. 2. Numerical results of a two-phase particle with dilational lithiation strain. (a) Radial distributions of Li concentration c, normalized by its maximum value at the fully lithiated state, and the radial distance r is normalized by the radius R of a partially lithiated particle, which increases as lithiation proceeds. (b) Radial distributions of the von Mises effective stress σ_e, radial stress σ_r and hoop stress $\sigma_\theta = \sigma_\varphi$, which corresponds to the Li concentration profile of (i) in (a). (c) Same as (b) except corresponding to the Li concentration profile of (ii) in (a). All the stress components are normalized by Young's modulus E.

spherical particle. Incidentally, the related discussion is also applicable to the hoop-stress buildup in the cross section of cylindrical wires [11]. In Fig. 3, the lithiation reaction front is represented by a sharp interface between a shrinking pristine core (white) and a growing lithiated shell (gray), as motivated by TEM observations. The shell is assumed to be fully lithiated with a constant Li concentration. It follows that the lithiation strain should be generated mainly near the moving core–shell interface, where the Li concentration changes abruptly.

Fig. 3a shows that, in the early stage of lithiation, element A is located within the pristine core. As lithiation occurs at the reaction front, the newly lithiated material at the front tends to move in the outward radial direction. This arises because there are larger areas in the hoop direction at larger radial distances, where the lithiation-induced volume expansion can be better accommodated with lower stresses generated. The outward displacement of newly lithiated materials results in hydrostatic tension in element A, as represented by stage (a) of the σ_θ curve in Fig. 3d. As the reaction front sweeps through element A, a large dilational lithiation strain is created at A. Owing to the constraint of surrounding material, local compressive stresses develop, such that element A sequentially undergoes tensile elastic unloading, compressive elastic loading and compressive plastic yielding in the hoop direction. This stress sequence is schematically represented by stage (b) in Fig. 3d. Interestingly, as the reaction front continues to move towards the center, the lithiation-induced swelling at the front pushes out the material behind it. This action causes further displacement of element A in the outward radial direction and simultaneously stretches it in the hoop directions (both σ_θ and σ_φ). As a result, element A experiences compressive elastic unloading, tensile elastic loading and tensile plastic yielding, which correspond to stage (c) in Fig. 3d. It is important to note that the tensile plastic flow in the surface layer could cause morphological instability and fracture of electrode particles during Li insertion, as shown in Fig. 1b.

It is noted that, during delithiation, the tensile hoop stress σ_θ should naturally arise owing to the constraint experienced by the delithiated material element, which tends to contract. However, it is somewhat unexpected to find that, during the lithiation of particles, the tensile σ_θ can also develop and even attain plastic yielding. As discussed earlier, this response results from continuous outward displacement of the material in the outer layer of the lithiated shell, driven by the large swelling at the core–shell interface, which progressively moves towards the center. Clearly, the finite curvature of the lithiated shell, large lithiation strain and plastic yielding are all essential to the reversal of the hoop compression to tension, i.e., from stage (b) to (c) in Fig. 3d. This is in contrast to the case of a flat phase boundary with zero curvature: i.e., the lithiation-induced compressive stresses, once developed at the phase boundary, will persist, since the material behind a flat moving boundary will not be strained further [22].

Finally, the results of stress generation given in this section were validated by direct finite element modeling, as described in the Appendix. Comparison between Figs. 2 and A1 indicates the overall consistency of the simulated Li profiles and associated stress distributions between the

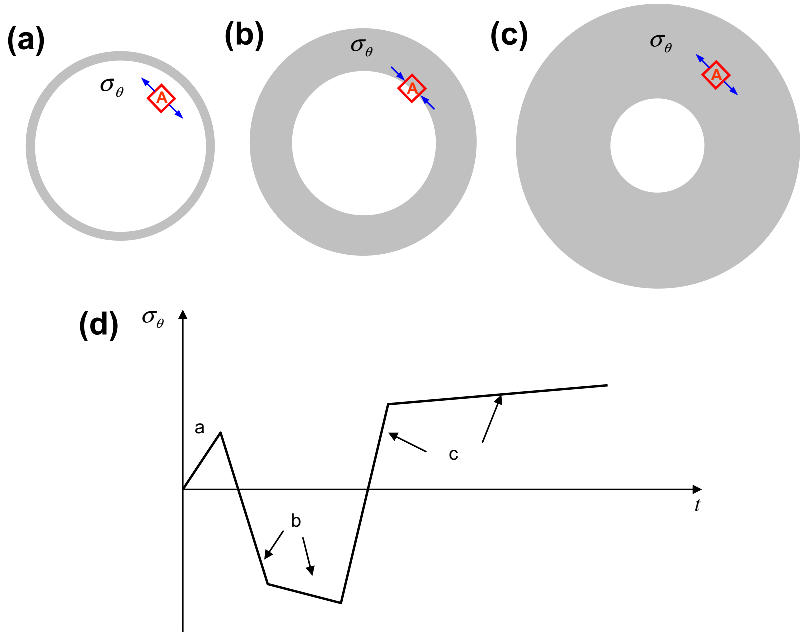

Fig. 3. Schematics showing how the hoop stress σ_θ changes in a spherical particle with a moving two-phase boundary between the pristine core (white) and lithiated shell (gray). (a–c) σ_θ in a representative material element A located at various distances relative to the moving phase boundary, i.e., core–shell interface. Progressive lithiation results in a gradual expansion of the particle. (d) σ_θ as a function of time t in element A.

two methods. The small numerical differences arise mainly because the small-strain approximation is used in the analytic formulation, while the large geometrical changes are accounted for in the finite element simulation in ABAQUS. Such differences indicate that the nonlinear geometrical changes will play an increasingly important role in the quantitative characterization of stress states as the chemical strain of lithiation increases. Nevertheless, the analytic formulation developed in Section 3 provides a transparent mechanics foundation for a more direct physical understanding of the lithiation-induced stress.

4.2. Single-phase particle

Existing models of diffusion-induced stress in the literature considered the Li diffusion in a single-phase particle or wire with a gradually varying Li distribution. Such single-phase lithiation models predicted only hoop compression in the surface layer (i.e., suppressing the fracture therein), and they also predicted hydrostatic tension in the center, where fracture was reasoned to first occur. Those results are in contradiction to the in situ TEM observation of fracture initiation from the Si particle surface.

Using the logistic function of Eq. (5), a gradual and smooth profile of Li distribution is also generated, mimicking the Li diffusion in a single-phase material, as studied in previous works. Fig. 4a shows the representative results of radial Li distributions by changing $B = 5$ in Eq. (5). The corresponding stress distributions are evaluated using the same method and the same set of constitutive parameters as the two-phase model. Fig. 4b and c shows the calculated radial stress distributions that correspond to the Li profiles in Fig. 4a. They are similar to the results given in a previous study [27]. Evidently, the hoop stress remains compressive in the outer layer of the single-phase particle as lithiation proceeds. This is in contrast to the development of surface hoop tension in the two-phase model, as shown in Fig. 2b and c.

To explain why the stress evolution in a single-phase particle is so different from that in a two-phase particle, it is noted that, in the former case, the Li concentration increases gradually from the particle center to its surface. The resultant stress states can be understood in terms of the competing effects of “differential expansion” and “push-out” associated with the curved phase boundary. First, consider two neighboring material elements. The one at a slightly larger radial distance always has a higher Li concentration than its neighbor, so as to drive the inward flow of Li. The concentration difference can result in expansion mismatch, and accordingly an additional compressive hoop stress in the former element relative to the latter. This mechanism of stress generation is due to the “differential expansion” effect. Next, focus on the stress history of a material element, called C, in the surface layer. As lithiation proceeds, the Li concentration in element C continuously increases, and so does the hoop compression as a result of the differential-expansion effect. However, a tensile hoop stress in element C could be induced by the “push-out” effect as a result of the volume expansion of materials away from element C (i.e., those at smaller radial distances relative to C). However, this tension is insufficient to offset the continuously increasing compressive stress caused by the differential-expansion effect, such that the hoop compression is retained within the surface layer in

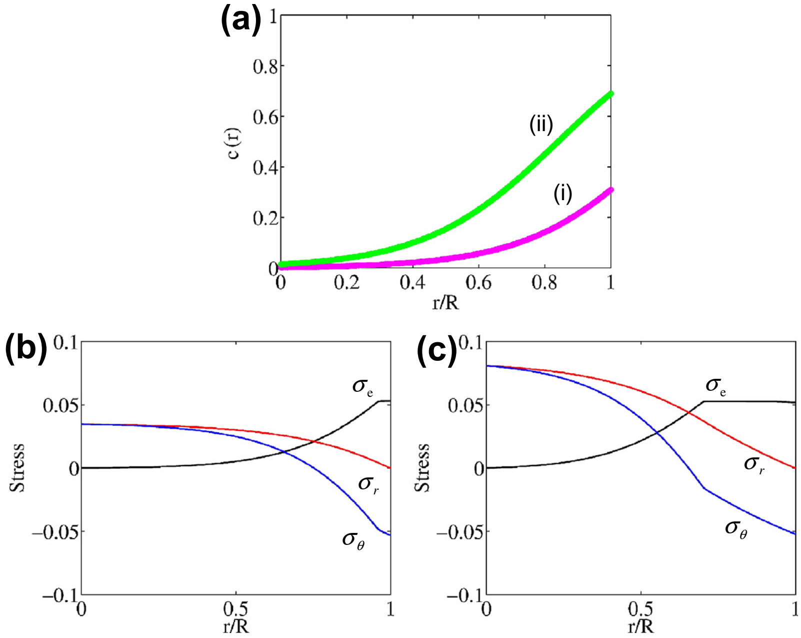

Fig. 4. Numerical results of a single-phase particle with dilational lithiation strain. (a) Radial distributions of normalized Li concentration c. (b) Radial distributions of the von Mises effective stress σ_e, radial stress σ_r and hoop stress $\sigma_\theta = \sigma_\varphi$ (normalized by Young's modulus E), which corresponds to the Li concentration profile of (i) in (a). (c) Same as (b) except corresponding to the Li concentration profile of (ii) in (a).

the single-phase particle. This is in contrast to the two-phase particle, where stressing due to the differential-expansion effect is only pronounced near the phase boundary, and the push-out effect is large enough to reverse the initial hoop compression into tension in the surface layer. Clearly, the large hoop tension in the outer layer provides the main driving force of surface cracking.

4.3. Dilational vs. unidirectional lithiation strain

Previous studies of oxidation-induced stresses have indicated that correct assignment of the oxidation strain is important for understanding the stress generation [46,48]. It has been noted that the assumed dilational oxidation strain would cause a large strain mismatch between the oxidized and unoxidized materials at a sharp phase boundary, where the oxygen concentration changes abruptly. To reduce the mismatch strain and associated strain energy, the reactive layer model [46] has been proposed, where the oxidation-induced swelling can become unidirectional along the normal direction of the phase boundary. It has been suggested that, during Si oxidation, the reactive layer can be as thin as a few atomic layers, and the oxidation occurs through a series of bond reconstructions within the layer. From the standpoint of the continuum mechanics modeling, such an interfacial process can be effectively represented by assigning a unidirectional oxidation strain to the material swept by the moving reactive layer. In other words, the oxidation-induced swelling in a particle can be assumed to occur only in the radial direction, normal to the core–shell interface, and further straining of the material behind the moving phase boundary is mainly caused by the push-out effect, as discussed earlier.

Motivated by the above analysis of the oxidation strains, the present authors studied the effect of radial/unidirectional lithiation strain on stress generation in a two-phase particle, while the exact atomic processes of strain transformation at the phase boundary are not yet clear [10]. In order to compare with the results obtained from the assumed dilational lithiation strain in Section 4.1, we take the same volume increase by ~100%, i.e., the lithiation expansion coefficients $\beta_r = 1$, and $\beta_\theta = \beta_\varphi = 0$. Fig. 5a and b shows the calculated stress distributions that correspond to the two Li profiles in Fig. 2a, respectively. In both plots, the approximate location of the phase boundary where the hoop stress begins to deviate from a constant value in the core can be identified.

Comparing Figs. 5a and b with 2b and c, the following similarities and differences in stress states are noticed between the cases of dilational vs. radial lithiation strains in a two-phase particle. As lithiation proceeds, the lithiated shell can readily achieve plastic yielding in both cases, underscoring the importance of plasticity in stress generation in the high-capacity electrode undergoing large lithiation-induced swelling. However, in the case of radial lithiation strain, Fig. 5 shows that the pristine core is subjected to hydrostatic compression. Within the lithiated shell, the hoop stress is compressive near the phase boundary, but it increases sharply and continuously, such that the tensile plastic yielding is achieved within a small radial distance, and the hoop tension further increases all the way to the particle surface. In contrast, in the case of dilational lithiation strain, Fig. 2b and c shows that the core is first subjected to hydrostatic tension, and later changed to hydrostatic compression as lithiation proceeds. Within the lithiated shell, near the phase boundary the hoop stress

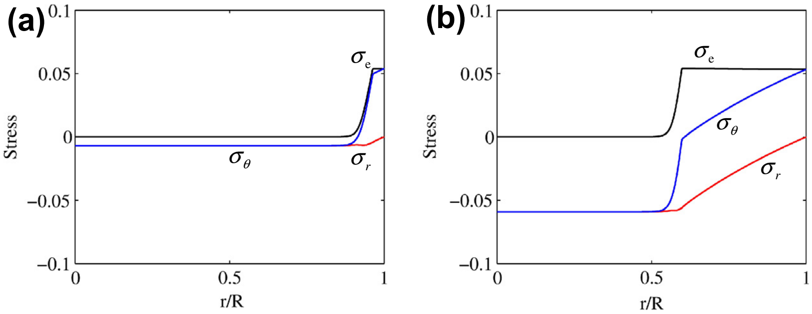

Fig. 5. Effects of the unidirectional lithiation strain on stress generation in a two-phase particle with the same radial distributions of Li as Fig. 2a. (a) Same as Fig. 2b except that the lithiation strain is unidirectional. (b) Same as Fig. 2c except the lithiation strain is unidirectional.

decreases sharply and almost discontinuously, such that the hoop stress becomes compressive, and plastic yielding is achieved. This hoop compression is reversed to tension at the larger radial distance as a result of the push-out effect, as discussed earlier.

The above results, regarding both the stress states in the core and near the phase boundary for the early stage of lithiation, agree qualitatively with those from an elastic model of oxidation-induced stresses [48], for cases of both radial and dilational lithiation strains. Hsueh and Evans [48] clearly explained why the core is subjected to hydrostatic compression in the case of radial oxidation strain, while the hydrostatic tension develops in the core in the case of dilational oxidation strain. Since a similar stress development is predicted in the early stage of lithiation, it is instructive to briefly review their explanations here. The key to understanding the stress buildup in the core is to first consider the deformation of the oxide (i.e., equivalent to the lithiated shell) in its “unconstrained” state, i.e., the oxide shell is assumed to detach from the core. In the case of dilational oxidation strain, the tangential component of the oxidation strain induces an unconstrained outward radial displacement, and the hydrostatic tension in the core results from the positive traction imposed to achieve displacement continuity at the core–shell interface. In contrast, the radial oxidation strain would induce the mixed tangential tension and compression in the unconstrained state of oxide. The hydrostatic compression in the core results from the negative traction imposed to achieve displacement continuity at the core–shell interface. Here, it should be noted that, while the analysis by Hsueh and Evans provides a direct physical appreciation of the stress states under different assumptions of oxidation strains, their work is only limited to elastic deformation. In contrast, the present model accounts for the plastic deformation that can readily develop during the lithiation of candidate high-capacity anode materials (Si, Ge, SnO_2), as shown in recent experiments [9,11–13].

Finally, note that both dilational and unidirectional lithiation strains represent the modeling limit of effective transformation strains associated with Li insertion at the sharp phase boundary. The main difference in the predicted stress states between the two cases lies in the compressive response near the reaction front, as discussed above. In fact, the contrast of the stresses in the core predicted by the two cases, i.e., hydrostatic tension vs. compression, suggests an experimental route of testing in which assumption of lithiation strain is more appropriate, e.g., by measuring the elastic lattice strain in the crystalline core through high-resolution TEM or electron diffraction experiments. Nevertheless, despite the different stress distributions between the two cases, the two-phase models can well capture the physical effect of large swelling at the phase boundary, i.e., hoop tension develops in the surface layer owing to the push-out effect, in a manner similar to inflation of a balloon causing its wall to stretch. The buildup of large hoop tension in the surface layer provides the main driving force of surface cracking, as observed in TEM experiments of Fig. 1b. In addition, note that the present authors’ recent comparative TEM study between Ge and Si nanoparticles suggested that the effect of anisotropy of lithiation strain could play a critical role in controlling the fracture of lithiated nanoparticles, i.e., being responsible for the tough Ge vs. fragile Si behaviors [49]. Further, recent TEM experiments [17,18] showed the two-phase lithiation in amorphous Si, which conceivably involves different degrees of anisotropy of lithiation strains compared with crystalline Si. These new results underscore the importance of physical understanding of the effect of anisotropy of lithiation strain.

5. Conclusions

This work studied the stress generation in a lithiated particle, accounting for both plastic deformation and the coexistence of Li-poor and Li-rich phases with a sharp and curved phase boundary. An analytic formulation of the problem was developed, and the stress distributions were solved using the finite difference method. Such development provides a transparent mechanics foundation for studying the lithiation-induced stresses in high-capacity electrode materials with multiphase microstructure, curved geometry and large volume change. The results show that the tensile hoop stress can develop in the lithiated shell even during Li insertion. This hoop tension originates from the lithiation-induced swelling at the sharp phase boundary with finite curvature, which often arises during lithiation of crystalline material with curved geometry, such as Si nanoparticles and nanowires. The large hoop tension in the outer layer can consequently trigger the morphological instability and fracture in electrodes. A recent study by Zhao et al. [36] obtained a similar result of tensile hoop stress development with a rigid-plastic model. However, the present results based on an elasto-plastic model are capable of resolving the stress distribution near the reaction front, which is necessary for understanding the coupling between stress and Li reaction/diffusion. For example, recent experiments showed the slowing of lithiation in Si nanoparticles and nanowires [38,39], and understanding such slowing requires knowledge of the coupling between stress and reaction/diffusion behind the reaction front. The present work also reveals how the predicted stress states are affected by different lithiation and deformation mechanisms, including the dilational vs. unidirectional lithiation strain, and the two-phase vs. single-phase lithiation mechanism. The results of lithiation-induced stresses provide a mechanics basis for further studying a wide range of lithiation-related phenomena, e.g., anisotropic swelling in Si nanowires [11], nanoporosity evolution in Ge nanowires [13], size effect on fracture in Si nanoparticles [14], and stress-retardation effect on lithiation [38,39].

Finally, it is noted that, in order to gain essential physical insights, the present model invokes various simplified assumptions. At this moment, for anodes with large volume and phase changes, it is probably more valuable to get the qualitative result and mechanism right (e.g., surface tensile stress and surface cracking, as opposed to surface compressive stress and bulk cracking) with a reduced model, than constructing a fully coupled model with a large set of parameters that have not been experimentally measured. Further, the present work is focused on the aspects of stress generation that are most likely insensitive to the rate effect, e.g., single-phase vs. two-phase lithiation. The present authors' recent review paper [50] addressed the rate effect by showing the consistent electrode degradation response between in situ TEM (conducted typically in the short time scale of ~10 min) and regular battery cell testing (conducted in hours). In addition, recent studies have begun to investigate the rate effect of reaction and diffusion on the lithiation behavior [37–40]. However, it is still uncertain whether the lithiation stress would dominantly retard the reaction or diffusion because of the limited availability of material parameters measured from experiments. In the future, it will be worthwhile to combine experiment and modeling to evaluate the impact of various factors, such as anisotropic properties of crystalline phases: e.g., orientation-dependent phase boundary mobility [11,51]; Li concentration-dependent properties, e.g., Young's modulus, yield strength, diffusivity [52,53]; stress relaxation by viscous flow [48,54]; coupling the stress with Li reaction and diffusion [26,30]. Ultimately, a mechanistic and quantitative understanding of the stress development holds the key to the control and mitigation of lithiation-induced fracture, thereby enabling the design of reliable Li ion batteries.

Acknowledgments

TZ acknowledges the support by NSF Grant CMMI-1100205. JL acknowledges the support by NSF DMR-1008104, DMR-0520020 and AFOSR FA9550-08-1-0325. SZ acknowledges the support by NSF Grant CMMI-1201058. The authors thank Drs. Jianyu Huang and Xiaohua Liu for stimulating discussions.

Appendix A. Finite element modeling

The present authors studied the evolution of a two-phase core–shell particle and associated stress generation using direct finite element simulations. Specifically, rather than using the logistic function given in Section 3.2, a non-linear diffusion model is employed for simulating the two-phase core–shell structure in the ABAQUS finite element package. To capture the coexistence of Li-poor and Li-rich phases, it was assumed that diffusivity D is non-linearly dependent on the local Li concentration c. Note that the diffusion simulations mainly serve to generate a sequence of core–shell structures for stress analysis, rather than provide a precise description of the dynamic lithiation process, which would be difficult owing to a lack of experimental measurements for model calibration. To this end, one takes a simple non-linear function of $D = D_0[1/(1-c) - 2\Omega c]$, where D_0 is the diffusivity constant, and Ω is tuned to control the concentration profile near the reaction front. On the basis of the free energy function of a regular solution model, $f = \Omega c(1-c) + [c \ln c + (1-c)\ln(1-c)]$, the above formula of diffusivity D is derived according to a definition that can sharply increase the diffusion rate at high Li concentrations: $D = D_0 c d^2 f / dc^2$. In diffusion simulations, the normalized Li concentrations behind the reaction front can quickly attain high values (slightly below 1), while those ahead of the front remain nearly zero. This produces a sharp reaction front that is consistent with experimental observation, thereby providing a basis for further stress analysis. It should be noted that a small gradient of lithium concentration still exists behind the reaction front, so that Li can continuously diffuse through the lithiated shell, so as to advance the reaction front toward the particle center. Finally, it is emphasized that the above non-linear diffusivity function is entirely empirical and taken as a numerical convenience for generating a sharp phase boundary for stress analyses. In future study, a mechanistically based model is needed to characterize both the phase boundary migration and Li diffusion. To this end, both quantitative experimental measurements and atomistic modeling of the related kinetic parameters are required to understand the migration of crystal/amorphous interfaces, as well as how Li diffuses in both Li-poor and Li-rich phases in Si electrodes.

The present authors numerically implemented both the above diffusion model and the elastic–plastic model in Section 2 in ABAQUS. The Li and stress–strain fields are solved with an implicit, coupled temperature–displacement

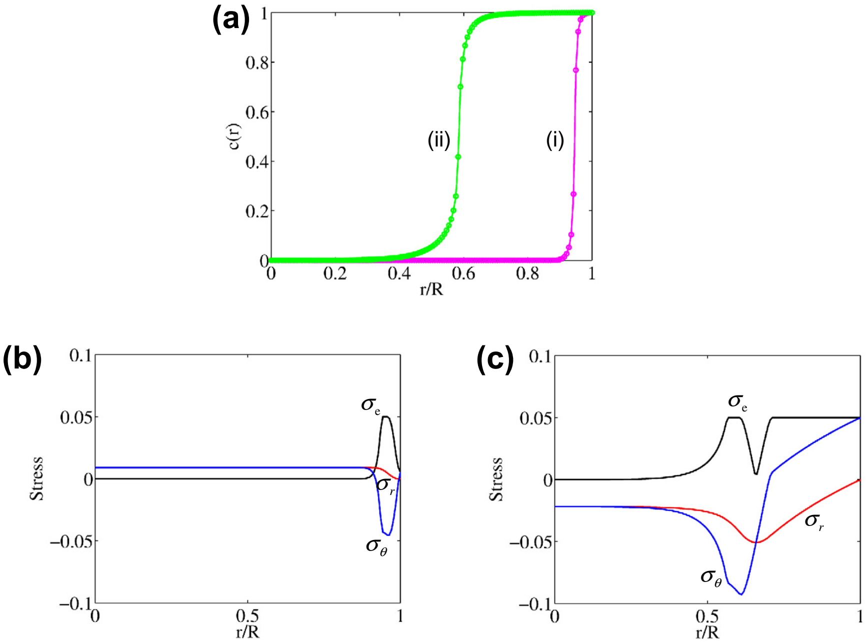

Fig. A1. Numerical results of a two-phase particle with dilational lithiation strain from finite element modeling. (a) Radial distributions of normalized Li concentration c. (b) Radial distributions of the von Mises effective stress σ_e, radial stress σ_r and hoop stress $\sigma_\theta = \sigma_\varphi$ (normalized by Young's modulus E), which corresponds to the Li concentration profile of (i) in (a). (c) Same as (b) except corresponding to the Li concentration profile of (ii) in (a).

procedure in ABAQUS/Standard. That is, the normalized concentration is surrogated by temperature, and the lithiation expansion coefficient β_{ij} is equivalently treated as the thermal expansion coefficient. The user material subroutine for heat transfer (UMATHT) is programmed to interface with ABAQUS to update diffusivities based on the current Li concentration (i.e., temperature). The Li distribution and accordingly elastic–plastic deformation are updated incrementally. In finite element simulations, one takes $\Omega = 1.95$ and assigns a constant Li concentration $c = 1$ at the surface; the alternative flux boundary condition gives similar results of stress generation. For numerical stability, the maximum of D is capped at $10^4 D_0$. The axisymmetric condition is used to reduce the computational cost in ABAQUS. In order to compare with the numerical results presented in the text, the same set of constitutive parameters is taken as that given in Section 4.1.

Fig. A1 shows the numerical results for a two-phase particle with dilational lithiation strain. They are consistent with Fig. 2. The small numerical differences arise mainly because the small-strain approximation is used in the analytic formulation, while the large geometrical changes are accounted for in the finite element simulation in ABAQUS by selecting the option of NLGEOM. In addition, the finite element modeling (not shown here) also validates the results with assumed radial lithiation strain in a two-phase particle given in Fig. 5. Clearly, the analytic formulation developed in Section 3 provides a transparent mechanics foundation for a more complete physical understanding of lithiation-induced stresses, while direct finite element modeling can be applied to solve the boundary value problems with complex geometries and chemo-mechanical loading histories.

References

[1] Tarascon JM, Armand M. Nature 2001;414:359.
[2] Whittingham MS. MRS Bull 2008;33:411.
[3] Goodenough JB, Kim Y. Chem Mater 2010;22:587.
[4] Huggins RA. Advanced batteries. New York: Springer; 2009.
[5] Beaulieu LY, Eberman KW, Turner RL, Krause LJ, Dahn JR. Electrochem Solid State Lett 2001;4:A137.
[6] Limthongkul P, Jang YI, Dudney NJ, Chiang YM. Acta Mater 2003;51:1103.
[7] Chan CK, Peng HL, Liu G, McIlwrath K, Zhang XF, Huggins RA, et al. Nat Nanotechnol 2008;3:31.
[8] Magasinski A, Dixon P, Hertzberg B, Kvit A, Ayala J, Yushin G. Nat Mater 2010;9:353.
[9] Sethuraman VA, Chon MJ, Shimshak M, Srinivasan V, Guduru PR. J Power Sources 2010;195:5062.
[10] Liu XH, Wang JW, Huang S, Fan F, Huang X, Liu Y, et al. Nat Nanotechnol 2012;7:749.
[11] Liu XH, Zheng H, Zhong L, Huang S, Karki K, Zhang LQ, et al. Nano Lett 2011;11:3312.
[12] Huang JY, Zhong L, Wang CM, Sullivan JP, Xu W, Zhang LQ, et al. Science 2010;330:1515.
[13] Liu XH, Huang S, Picraux ST, Li J, Zhu T, Huang JY. Nano Lett 2011;11:3991.
[14] Liu XH, Zhong L, Huang S, Mao SX, Zhu T, Huang JY. ACS Nano 2012;6:1522.
[15] Liu XH, Huang JY. Energy Environ Sci 2011;4:3844.
[16] Chon MJ, Sethuraman VA, McCormick A, Srinivasan V, Guduru PR. Phys Rev Lett 2011;107:045503.
[17] Wang JW, He Y, Fan F, Liu XH, Xia S, Liu Y, et al. Nano Lett 2013;13:709.
[18] McDowell MT, Lee SW, Harris JT, Korgel BA, Wang C, Nix WD, et al. Nano Lett 2013;13:758.

[19] Chandrasekaran R, Magasinski A, Yushin G, Fuller TF. J Electrochem Soc 2010;157:A1139.
[20] Ryu I, Choi JW, Cui Y, Nix WD. J Mech Phys Solids 2011;59:1717.
[21] Zhang XC, Shyy W, Sastry AM. J Electrochem Soc 2007;154:A910.
[22] Huggins RA, Nix WD. Ionics 2000;6:57.
[23] Christensen J, Newman J. J Solid State Electrochem 2006;10:293.
[24] Cheng YT, Verbrugge MW. J Power Sources 2009;190:453.
[25] Bhandakkar TK, Gao HJ. Int J Solids Struct 2011;48:2304.
[26] Bower AF, Guduru PR, Sethuraman VA. J Mech Phys Solids 2011;59:804.
[27] Zhao KJ, Pharr M, Vlassak JJ, Suo ZG. J Appl Phys 2011;109:016110.
[28] Tang M, Huang HY, Meethong N, Kao YH, Carter WC, Chiang YM. Chem Mater 2009;21:1557.
[29] Burch D, Bazant MZ. Nano Lett 2009;9:3795.
[30] Gao YF, Zhou M. J Appl Phys 2011;109:014310.
[31] Golmon S, Maute K, Lee SH, Dunn ML. Appl Phys Lett 2010;97:033111.
[32] Deshpande R, Cheng YT, Verbrugge MW, Timmons A. J Electrochem Soc 2011;158:A718.
[33] Cui Z, Gao F, Qu J. J Mech Phys Solids 2012;60:1280.
[34] Yang H, Huang S, Huang X, Fan FF, Liang WT, Liu XH, et al. Nano Lett 2012;12:1953.
[35] Bhandakkar TK, Johnson HT. J Mech Phys Solids 2012;60:1103.
[36] Zhao KJ, Pharr M, Wan Q, Wang WL, Kaxiras E, Vlassak JJ, et al. J Electrochem Soc 2012;159:A238.
[37] Pharr M, Zhao K, Wang X, Suo Z, Vlassak JJ. Nano Lett 2012;12:5039.
[38] McDowell MT, Ryu I, Lee SW, Wang C, Nix WD, Cui Y. Adv Mater 2012;24:6034.
[39] Liu XH, Fan F, Yang H, Zhang S, Huang JY, Zhu T. ACS Nano 2013;7:1495.
[40] Cui ZW, Gao F, Qu JM. J Mech Phys Solids 2013;61:293.
[41] Kasavajjula U, Wang CS, Appleby AJ. J Power Sources 2007;163:1003.
[42] Zhu T, Li J. Prog Mater Sci 2010;55:710.
[43] Gao HJ, Ji BH, Jager IL, Arzt E, Fratzl P. Proc Natl Acad Sci USA 2003;100:5597.
[44] Chen LQ. Annu Rev Mater Res 2002;32:113.
[45] Wang YZ, Li J. Acta Mater 2010;58:1212.
[46] Mott NF, Rigo S, Rochet F, Stoneham AM. Philos Mag B 1989;60:189.
[47] Haghi M, Anand L. Int J Plast 1991;7:123.
[48] Hsueh CH, Evans AG. J Appl Phys 1983;54:6672.
[49] Liang W, Yang H, Fan F, Liu Y, Liu XH, Huang JY, et al. ACS Nano 2013;7:3427.
[50] Liu XH, Liu Y, Kushima A, Zhang SL, Zhu T, Li J, et al. Adv Energy Mater 2012;2:722.
[51] Goldman JL, Long BR, Gewirth AA, Nuzzo RG. Adv Funct Mater 2011;21:2412.
[52] Shenoy VB, Johari P, Qi Y. J Power Sources 2010;195:6825.
[53] Huang S, Zhu T. J Power Sources 2011;196:3664.
[54] Kao DB, McVittie JP, Nix WD, Saraswat KC. IEEE Trans Electron Dev 1988;35:25.